

Characterization of mammographic masses using a gradient-based segmentation algorithm and a neural classifier

Pasquale Delogu^a, Maria Evelina Fantacci^a, Parnian Kasae^b
and Alessandra Retico^{a*}

^a Dipartimento di Fisica dell'Università di Pisa and INFN Sezione di Pisa,
Largo Pontecorvo 3, 56127 Pisa, Italy.

^b The Abdus Salam International Center for Theoretical Physics,
Strada Costiera 11, P.O. Box 563, 34100 Trieste, Italy.

Abstract

Computerized methods have recently shown a great potential in providing radiologists with a second opinion about the visual diagnosis of the malignancy of mammographic masses. The computer-aided diagnosis (CAD) system we developed for the mass characterization is mainly based on a segmentation algorithm and on the neural classification of several features computed on the segmented mass. Mass-segmentation plays a key role in most computerized systems. Our technique is a gradient-based one, showing the main characteristic that no free parameters have been evaluated on the dataset used in this analysis, thus it can directly be applied to datasets acquired in different conditions without any ad-hoc modification.

A dataset of 226 masses (109 malignant and 117 benign) has been used in this study. The segmentation algorithm works with a comparable efficiency both on malignant and benign masses. Sixteen features based on shape, size and intensity of the segmented masses are extracted and analyzed by a multi-layered perceptron neural network trained with the error back-propagation algorithm. The capability of the system in discriminating malignant from benign masses has been evaluated in terms of the receiver-operating characteristic (ROC) analysis. A feature selection procedure has been carried out on the basis of the feature discriminating power and of the linear correlations interplaying among them. The comparison of the areas under the ROC curves obtained by varying the number of features to be classified has shown that 12 selected features out of the 16 computed ones are powerful enough to achieve the best classifier performances. The radiologist assigned the segmented masses to three different categories: *correctly*-, *acceptably*- and *non-acceptably-segmented* masses. We initially estimated the area under ROC curve only on the first category of segmented masses (the 88.5% of the dataset), then extending the classification to the second subclass (reaching the 97.8% of the dataset) and finally to the whole dataset, obtaining $A_z = 0.805 \pm 0.030, 0.787 \pm 0.024$ and 0.780 ± 0.023 , respectively.

Keywords: Computer-aided diagnosis, breast cancer, mammography, image processing, segmentation, neural networks.

Introduction

Breast cancer is still one of the most common forms of cancer among women, despite earlier detection and more effective treatments have contributed to a significant decrease in the breast-cancer mortality during the last decades [1–4]. Mammography

*Corresponding author: Alessandra Retico, Ph.D.; E-mail: alessandra.retico@df.unipi.it

is widely recognized as the most reliable technique for early detection of breast cancers [5, 6]. Once a mass is detected on a mammogram, the radiologist recommends further investigations, depending on the probability of malignancy he assigns to that lesion. However, the characterization of masses from mammographic images is a very difficult task and a high number of unnecessary biopsies are actually performed in the routine clinical activity. The rate of positive findings for cancers at biopsy ranges from 15% to 30% [7], i.e. the specificity in differentiating malignant from benign lesions on mammographic images is rather low. As a breast biopsy is an invasive and expensive procedure, methods to improve mammographic specificity without missing cancer have to be developed. A higher predictive rate of the mammographic examination can be achieved by combining the radiologist's interpretation and the computer analysis. Computerized methods have recently shown a great potential in assisting radiologists in the malignant or benign decision, by providing them with a second opinion about the visual diagnosis of the lesion [8–10].

The computer-aided diagnosis (CAD) system for characterizing masses described in this paper is based on a three-stage algorithm: first, a segmentation technique extracts the mass from the image; then, several features based on size and shape of the lesion are computed; finally, a neural classifier merges the features into a likelihood of malignancy for that lesion. With respect to a number of CAD systems with a similar purpose and using a similar approach already discussed in the literature, the system we present shows the distinguishing characteristic that a robust segmentation technique has been implemented: it is based on a segmentation algorithm completely free from any application-dependent parameter.

This paper is structured as follows: the methodology is presented in sec. 1, sec. 2 describes the mammographic dataset available for our study and sec. 3 reports on the analysis details and on the whole system performances.

1 Methodology

1.1 Mass segmentation

Mass segmentation is a quite difficult task because masses are often varying in size, shape and density. Masses can exhibit a very poor image contrast or can be highly connected to the surrounding parenchymal tissue. Thus, it is hard in many cases to distinguish the mass from the nonuniform normal breast tissue. Due to the high variability in the appearance of masses, generalizing a segmentation algorithm able to handle many different types of masses is a nontrivial task and much efforts have already gone through this issue [11–15].

The segmentation algorithm we developed is an extension and a refinement of the strategy proposed in [16] for the mass segmentation in the CAD analysis of breast tumors on sonograms. The procedure we propose is able to identify the mass shape within a Region Of Interest (ROI) the radiologist interactively chooses on the mammogram. Despite the radiologist is asked to select the smallest region containing the mass, the ROIs usually contain the lesions as well as a considerable part of normal tissue. Our segmentation method aims at removing the non-tumor regions around the tumor in a ROI by applying the following processing steps (see fig. 1).

Step 1. Once the ROI containing the mass has been selected by the physician, a shrinking factor of 8 is applied on both rows and columns within the rectangular region both to reduce the high-frequency noise affecting the digitized images and to limit the segmentation computing time.

Step 2. Assuming that masses become denser and denser as going from the boundary to the center, we took the pixel with the maximum-intensity value as the starting point for the segmentation algorithm (seed point). Since the ROI can even contain pixels belonging to the normal tissue with higher intensity values with respect to the pixels representing the mass, the center of the ROI is taken as the seed point if the distance between the maximum-intensity pixel and the center of the ROI

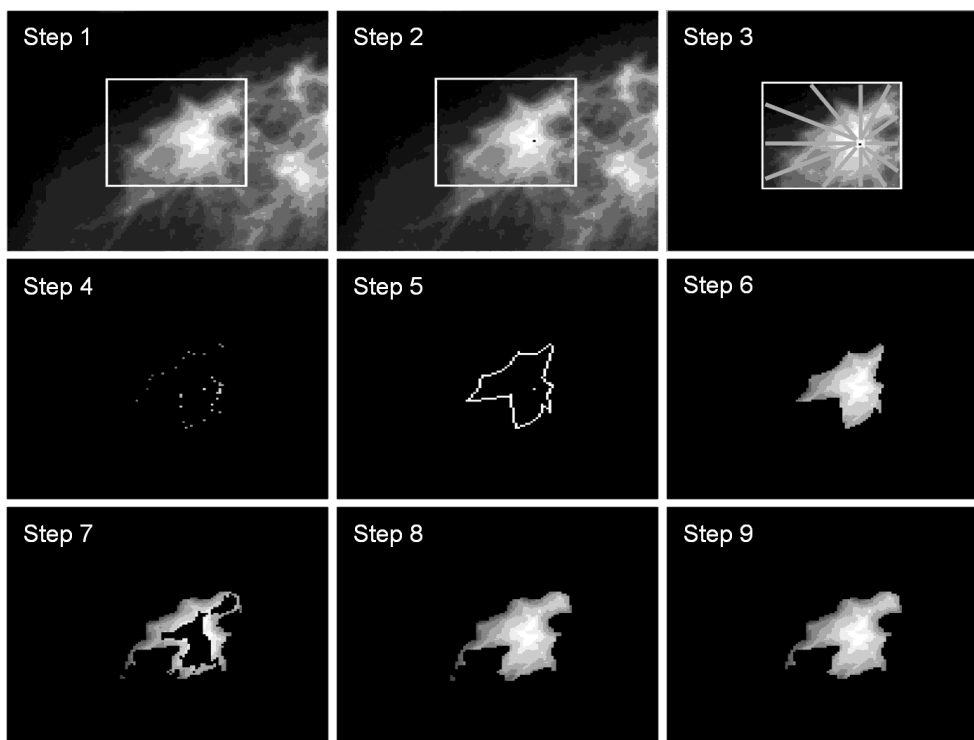


Figure 1: Mass segmentation procedure: for the explanation of the algorithms implemented in each single step see the text.

exceed the 75% of the ROI half diagonal¹.

Step 3. A number of radial lines are depicted from the chosen seed point to the boundary of the ROI area.

Step 4. We scan the pixels along each radial line starting from the center to the boundary of the ROI. We look for the pixel whose local variance is maximal. The local variance is defined as the variance in a predefined $n \times n$ matrix with the currently processed pixel in the center. The pixel with the maximal local variance is considered to be most likely the boundary point between the mass and the surrounding tissue: it is referred in what follows as critical point. The smaller the size of the matrix we consider, the more sensitive to the small variances or details. This can be a helpful parameter for detecting the arms and branches of the stellate masses. Both to enhance the sensitivity of the segmentation procedure to small details of the lesions and to reduce the algorithm execution time, the smallest size of the pixel neighborhood has been chosen in the computation of the local variance, i.e. $n = 3$.

Step 5. After scanning all radial lines and finding the critical points corresponding to each one of them, the critical points are linearly interpolated.

Step 6. The region inside the coarse boundary so far identified is filled. We use the pixels of this region as seed points for the further steps of the segmentation algorithm, whose aim is to lead to a more detailed and more accurate identification of the shape of the lesion.

Step 7. The steps 3 and 4 are iterated for each seed point identified in the step 6. What we obtain is a set of points detected from different angles to be most probably located on the boundary. In order to select the right thin boundary out of this set, we first tried to assign a vote to the pixel detected at each time as a critical

¹As the ROI is a user-drawn rectangle containing the mass, the center of the ROI and the center of the lesion are not expected to be very different.

point so that the higher the credit of the critical point, the higher the probability of being appropriate to represent the real boundary of the mass. We found out that selecting appropriate criteria for assigning and thresholding the votes was crucial for the mass border identification and led to disconnectivity. Therefore, in order to avoid the unnecessary presence of free application-dependent parameters in this procedure we decided to accept all identified points. In this way we will end up with a thick and more connected border.

Step 8. To complete the identification of the mass, the area inside the border has to be filled. Since we may have self-intersecting region it is more convenient to fill the background. To prevent entering the mass from possible disconnectivity in the border we use a cross-like mask for filling background. Subtracting filled background from ROI will give the mass.

Step 9. A final filtering is performed in order to remove some possibly present non-connected objects.

1.2 Feature extraction

Once the masses have been segmented out from the surrounding normal tissue, a set of morphological and textural features are computed in order to allow a decision-making system to distinguish benign from malignant lesions. The likelihood of malignancy for a mass can in fact be estimated on the basis of its morphological and textural appearance, which is usually described in terms of the mass size, shape, margin characteristics and x-ray attenuation (radio-density) [17–24].

Despite mass size alone does not predict malignancy, the size of a malignant mass is indicative of its progression. Therefore features like *area* and *perimeter* are usually included in the set of features to be computed.

The mass shape can be round, oval, lobular or irregular. Features like: *circularity*, *convexity*, *maximum axis*, *minimum axis* can be useful in mass malignancy definition since most benign masses appear circular and convex whereas malignant cases have irregular non-convex shapes.

The study of the mass margin characteristics is probably the most important in determining whether the mass is likely to be benign or malignant. There are five type of mass margins as defined by BI-RADS® [25]: circumscribed, obscured, microlobulated, ill-defined, and spiculated. Circumscribed margins are well defined and sharply demarcated with an abrupt transition between the lesion and the surrounding tissue. Microlobulated margins have small undulating circles along the edge of the mass. Obscured margins are hidden by superimposed or adjacent normal tissue. Ill-defined margins are poorly defined and scattered. Spiculated margins are marked by radiating thin lines. The features which can estimate the level of spiculations and evaluate the softness or roughness of the margin are: *mean and standard deviation of normalized radial length*, *radial length entropy*, *zero crossing*, *mean and standard deviation of the variation ratio*.

The X-ray attenuation is a description of the density of the mass. Breast cancer often appears denser, i.e. whiter, than the surrounding normal breast parenchyma. The intensity and its variation inside the mass can be measured by features like: *mean*, *standard deviation*, *kurtosis* and *skewness of the mass intensity*.

Supported by the existing correlations between the morphological and textural features of a mass and its likelihood of malignancy, we computed the already mentioned 16 features on segmented masses according to the following formulas.

1. **Mass Area:** it is given by the number of pixels inside the boundary of the mass.
2. **Mass Perimeter:** it is measured by summing up the number of pixels on the boundary of the mass.
3. **Circularity:**

$$C = \frac{4\pi A}{P^2}, \quad (1)$$

where P is the perimeter and A is the area of the mass. The circularity C is calculated in such a way that for a mass with circular shape $C = 1$. Changing the shape to oval or irregular this number decreases.

4. **Mean of the Normalized Radial Length:**

$$d_{\text{avg}} = \frac{1}{P} \sum_{i=1}^P d(i), \quad (2)$$

where $d(i)$ is the Euclidean distance from the center of mass of the segmented lesion to the i^{th} pixel on the mass boundary and normalized with respect to the maximum distance found for that mass. P is the mass perimeter.

5. **Standard Deviation of Normalized Radial Length:**

$$\sigma = \sqrt{\frac{1}{P} \sum_{i=1}^P (d(i) - d_{\text{avg}})^2}. \quad (3)$$

It is a good measure for irregularity. The more spiculations and irregularities are present, the higher is the standard deviation of the radial length.

6. **Radial Length Entropy:** it is a probabilistic measure computed from the histogram of the normalized radial length as follows:

$$E = - \sum_{k=1}^{N_{\text{bins}}} P_k \log P_k. \quad (4)$$

The parameter P_k is the probability that the normalized radial length is between $d(i)$ and $d(i) + 1/N_{\text{bins}}$, where N_{bins} is the number of bins the normalized histogram, ranging in the $[0,1]$ interval, has been divided in ($N_{\text{bins}} = 5$ in our analysis).

7. **Zero Crossing:** it is a count of the number of times the radial distance plot crosses the average radial distance. It is an indicator for the degree of spiculation of the mass.
8. **Maximum Axis:** it consists is the largest distance connecting one point along the mass boundary to another point on the mass boundary going through the center of mass of the lesion.
9. **Minimum Axis:** it is the shortest distance connecting one point along the mass boundary to another point on the mass boundary going through the center of mass of the lesion.
10. **Mean of the Variation Ratio:** first we find the variation of all radial length from their mean value, then we determine the maximum variation magnitude var_{max} of radial length. Only those variations having a magnitude greater than $var_{\text{max}}/2$ are considered as dominant variations. The variation ratio mean is computed as the average of those dominant variations.
11. **Standard Deviation of the Variation Ratio:** it is calculated as the standard deviation of the dominant variations with respect to the variation ratio mean. It indicates the sharpness of the variations and can be a good indicator for spiculation.
12. **Convexity:** it is the ratio between the mass area and the area of the smallest convex containing the mass. If the mass has a regular shape, which means it is convex, this number is one, otherwise it will decrease.
13. **Mean of the Mass Intensity:** it is the mean value of the grey-level intensity values of the pixels inside the mass boundaries.
14. **Standard Deviation of the Mass Intensity:** it is a measure of the smoothness of the grey-level intensity values of the pixels inside the mass boundaries.

15. **Kurtosis of the Mass Intensity:** it is a measure of how outlier-prone is a distribution. It is defined as follows:

$$kurtosis = \frac{E(g(i, j) - \mu)^4}{\sigma^4}, \quad (5)$$

where $g(i, j)$ is the grey level at location (i, j) , μ and σ are the average intensity and standard deviation inside the segmented mass, respectively. We can investigate how far is the intensity distribution of the mass from a normal distribution. The *kurtosis* of the normal distribution is 3. Distributions that are more outlier-prone than the normal distribution have a *kurtosis* greater than 3; distributions that are less outlier-prone have a *kurtosis* lower than 3.

16. **Skewness of the Mass Intensity:** it is a measure of the asymmetry of the data around the sample mean. It is given by:

$$skewness = \frac{E(g(i, j) - \mu)^3}{\sigma^3}. \quad (6)$$

If the *skewness* is negative, the data are spread out more to the left of the mean than to the right. If it is positive, the data are spread out more to the right. The *skewness* of a normal distribution or a perfectly symmetric distribution is zero.

1.3 Classification

Once the features are extracted from the segmented masses, one faces with the choice of an appropriate classification method. Lots of different approaches implemented to this purpose have been widely discussed in literature, such as the *Minimum Distance Classifier* [26, 27], the *K-Nearest Neighbor Distance Classifier* [26], the *Linear Discriminant Method (LDA)* [13, 27, 28, 33], the *K-mean clustering* [26], the *Binary Classification Tree* [29] and *Artificial Neural Network (ANN)* [17, 30–32, 34]. Neural networks are widely used because of their capability of simultaneously processing large amounts of information, for their ability in analyzing and classifying patterns even when presented with noisy or partial information and to adapt their behavior to the nature of the training data.

Relying on the advantages of a neural approach, we implemented a supervised neural classifier in our CAD scheme. A standard three-layer feed-forward neural network [35] has been chosen to this purpose. The general architecture of this ANN consists in n input, h hidden and two output neurons, and the supervised training phase is based on the back-propagation algorithm. We used the sigmoid activation function for both the hidden layer and the output layer, and the on-line learning method allowing weights to be updated after the presentation of each pattern. Updating was synchronous, therefore all nodes were updated at the same time. The supervised learning is performed by showing the network a set of training vectors constituted by the input pattern and the corresponding target response. In particular, the target $[1, 0]$ has been added to the vectors of features extracted from malignant masses, whereas the target $[0, 1]$ to those derived from benign masses. Let us assume $[y_1, y_2]$ to be the output of the network for a given input: the corresponding lesion is classified as malignant if $y_1 > y_2$, otherwise it is assumed to be benign. Whereas the number n of units in the input layer is *a priori* fixed by the choice of the number of features to be classified, the number h of hidden neurons has to be experimentally determined on the basis of the training dataset.

The performances of the training algorithm were evaluated according to the 5×2 cross validation method [36]. It is the recommended test to be performed on algorithms that can be executed 10 times because it can provide a reliable estimate of the variation of the algorithm performances due to the choice of the training set. This method consists in performing 5 replications of the 2-fold cross validation method [37]. At each replication, the available data are randomly partitioned into 2 sets (A_i and B_i for $i = 1, \dots, 5$) with an almost equal number of entries. The learning algorithm is trained on each set and tested on the other one. The performances the system achieves in the classification phase are given in terms of the sensitivity and specificity values. The

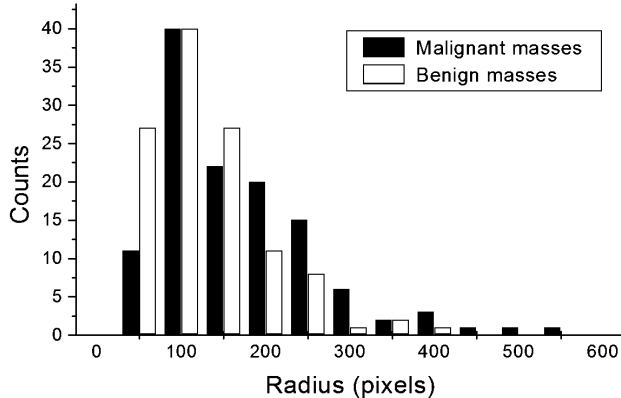


Figure 2: Distribution of the mass sizes: the radius of the *truth circles* annotated by experienced radiologists are shown for malignant and benign masses.

sensitivity is defined as the true positive fraction (fraction of malignant masses correctly classified by the system), whereas the specificity is referred to the true negative fraction (fraction of benign masses correctly classified by the system).

The performances of the neural classifier were also evaluated in terms of a Receiver Operating Characteristic (ROC) analysis [38]. In order to show the trade off between the sensitivity and the specificity, a ROC curve is obtained by plotting the true positive fraction versus the false positive fraction of the cases ($1 - \text{specificity}$), computed while the decision threshold of the classifier is varied. Each decision threshold results in a corresponding operating point on the curve, which usually goes through the points $(0, 0)$, where the classifier detects no positives, and $(1, 1)$, where every pattern is classified as positive.

2 Image data set

The image data set used for this study has been extracted from a large database of mammograms collected in the framework of a Collaboration between physicists from several Italian Universities and INFN (Istituto Nazionale di Fisica Nucleare) Sections, and radiologists from several Italian Hospitals [39, 40]. The mammograms come both from screening and from the routine work carried out in the participating Hospitals. The $18 \times 24 \text{ cm}^2$ mammographic films were digitized by a CCD linear scanner (Linotype Hell, Saphir X-ray). The digitized images are characterized by a $85 \mu\text{m}$ pixel pitch and a 12-bit resolution, thus allowing up to 4096 grey levels. The pathological images are fully characterized by a consistent description, including the radiological diagnosis, the histological data and the coordinates of the center and the approximate radius (in pixel units) of a circle enclosing the masses (*truth circle*). Mammograms with no sign of pathology are stored as normal images only after a follow up of at least three years.

A set of 226 masses were used in this study: 109 malignant and 117 benign masses were extracted from single-view cranio-caudal or lateral mammograms. The distribution of the mass sizes can be observed in fig. 2, where the histograms of the radius in pixels of the *truth circles* indicating the pathological regions, as annotated by experienced radiologists, are shown for the malignant and benign cases. The diameters of the *truth circles* in real units are in the range 6.6–94.4 mm. It is worth noting that the size of the *truth circle* usually overestimates the real size of the mass. The dataset we analyzed can be considered as representative of the patient population that is sent for biopsy under the current clinical criteria.

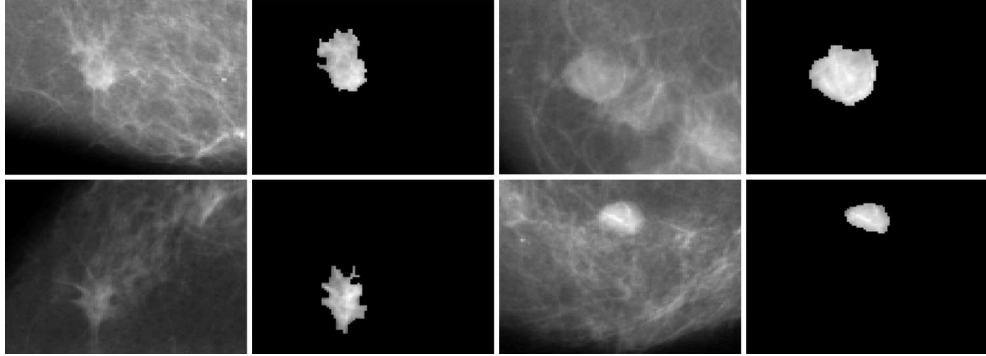


Figure 3: Examples of *correctly-segmented* masses: two malignant masses on the left and two benign masses on the right.

3 Results

3.1 Segmentation Result

The segmentation algorithm efficiency was directly evaluated with the assistance of an experienced radiologist who, after selecting the ROI to be analyzed ², assigned the masses automatically segmented by the system to one out of the following three categories: *correctly-segmented*, *acceptably-segmented* or *non-correctly-segmented* masses.

The radiologist has been asked to classify as *correctly segmented* only those masses whose identified boundary was sufficiently close to that she would have drawn by hand on the image. Despite the borders of the masses are usually not very sharp in mammographic images, the segmentation procedure we propose leads in most cases to a quite accurate identification of the mass shapes (see fig. 3). In fact, 200 masses (95 malignant and 105 benign) out of the dataset of 226 cases, were correctly segmented leading to an efficiency of correct segmentation $\epsilon_{CS} = 88.5\%$. Out of the 26 remaining cases, 21 masses were assigned to the category of *acceptably-segmented* masses, whereas 5 masses were definitely rejected by the radiologist as *non-correctly-segmented* cases. Some examples of reasonably segmented masses are shown in fig. 4. It can be noticed that these masses are usually characterized by an obscured margin or they are not fully visible in the available mammographic field of view. In such cases the interactive selection of an appropriate ROI becomes particularly difficult and user-dependent, ending up with a non-satisfactory identification of at least a portion of the mass margin. In case of *non-correctly-segmented* masses a too large portion of the mass margin is not correctly identified. If the *acceptably-segmented* masses are added to the set of *correctly-segmented* masses the fraction of the dataset of masses that will be analyzed and classified by the CAD system will reach the value $\epsilon_{CS+AS} = 97.8\%$.

3.2 Analysis of the extracted features

Despite each of the 16 features we computed on the segmented masses can potentially enlighten a different characteristic of a mass and contribute to a good classification result, we performed some tests to evaluate the discriminatory power of each feature and the degree of linear correlation among the different features. We restricted this analysis to the feature extracted from the 200 *correctly-segmented* masses.

²The current CAD GUI allows the radiologist to select a maximum area of 1000×1000 pixels on the digitized mammogram. Despite this technical restriction could easily be removed, it does not affect the current analysis as the maximum actual size of the larger mass in our database is less than 1000 pixels. The disagreement of this statement with the histogram reported in fig. 2 is only apparent because the radiologist's *truth circles* are usually very conservative; a factor of 0.8 ± 0.3 actually occurs between half of the maximum mass axis (computed on the segmented masses and confirmed by an experienced radiologist) and the radiologist's annotated mass radius for the *truth circles*.

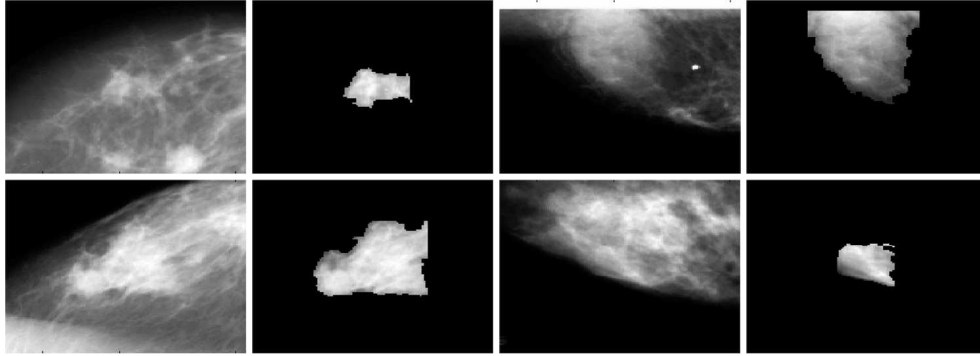


Figure 4: Examples of *acceptably-segmented* masses: two malignant masses on the left and two benign masses on the right.

The distributions of the features computed for the malignant and benign cases are plotted in figures 5 and 6³. The mean values of the features extracted from malignant and benign masses show highly significant differences (p -values < 0.01) for 13 features out of the 16 we computed. For one of the remaining features (the *kurtosis of the intensity*) the means are significantly different ($p < 0.05$). The only two features not showing a significant difference in the mean values are the *mean of variation ratio* and the *skewness of the intensity*.

The analysis of the linear correlations $\rho(i, j)$ among the 16 features (see the matrix of the correlation coefficients in tab. 1), lead to the following considerations:

- the *perimeter* is highly correlated to the *zero crossing*, the *maximum axis*, the *minimum axis* and the *area*; if the *perimeter* is excluded from the feature set, the correlations among the remaining features all satisfy the constraint $\rho(i, j) < 0.93$;
- if we set the threshold $\rho(i, j) < 0.9$ on the correlation coefficients we have to exclude from the set also the *radial length entropy*, the *maximum axis* and the *minimum axis* ending up with 12 remaining features.

On the basis of these preliminary analysis on the features, we decided to select the optimal set of features to be finally computed by the CAD system by comparing the neural network performances obtained with different choices of the feature set cardinality.

3.3 Classification

We prepared 5 different train and test sets for the 5×2 cross validation analysis, by randomly assigning each of the 200 vectors of features to the train or test set for each of the 5 different trials.

We trained 4 different sets of 10 networks by varying the number of features taken into account for the classification:

- a) all 16 features are considered;
- b) 15 features are considered (the *perimeter*, which has the higher correlations with other features, is excluded);
- c) 14 features are considered (the *mean value of variation ratio* and the *skewness of the intensity* are excluded, as they have the poorest discriminating power);
- d) 12 features are considered (the *perimeter*, the *radial length entropy*, the *maximum axis* and the *minimum axis* are excluded, as they have $\rho(i, j) > 0.9$ with some other features);

³Notice that the shrinking factor of 8 applied to both rows and columns of the original image has not been taken into account in drawing the distributions of the quantities measured in pixel units.

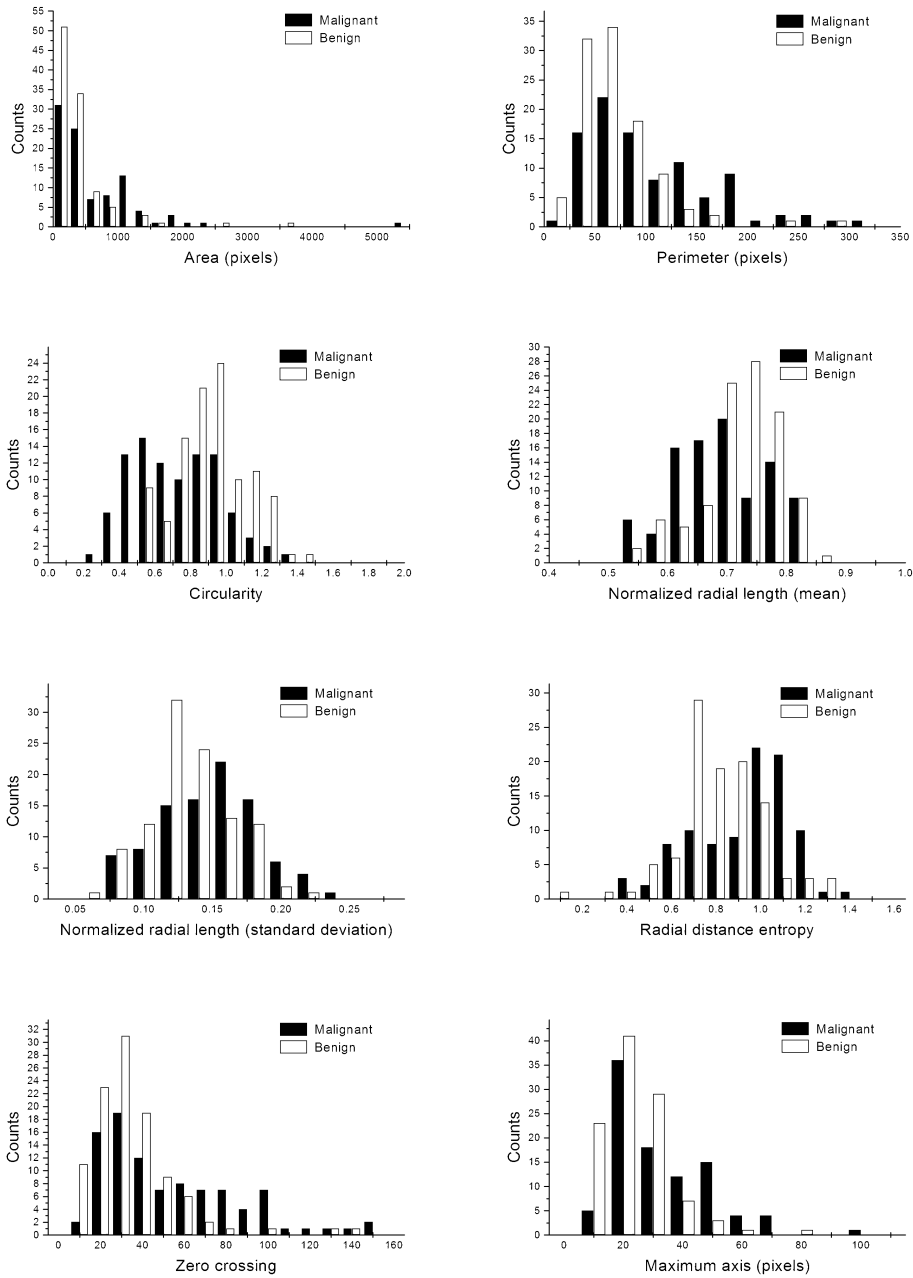


Figure 5: Distributions of the following features computed for malignant and benign masses: *area; perimeter; circularity; mean and standard deviation of normalized radial length; radial distance entropy; zero crossing; maximum axis.*

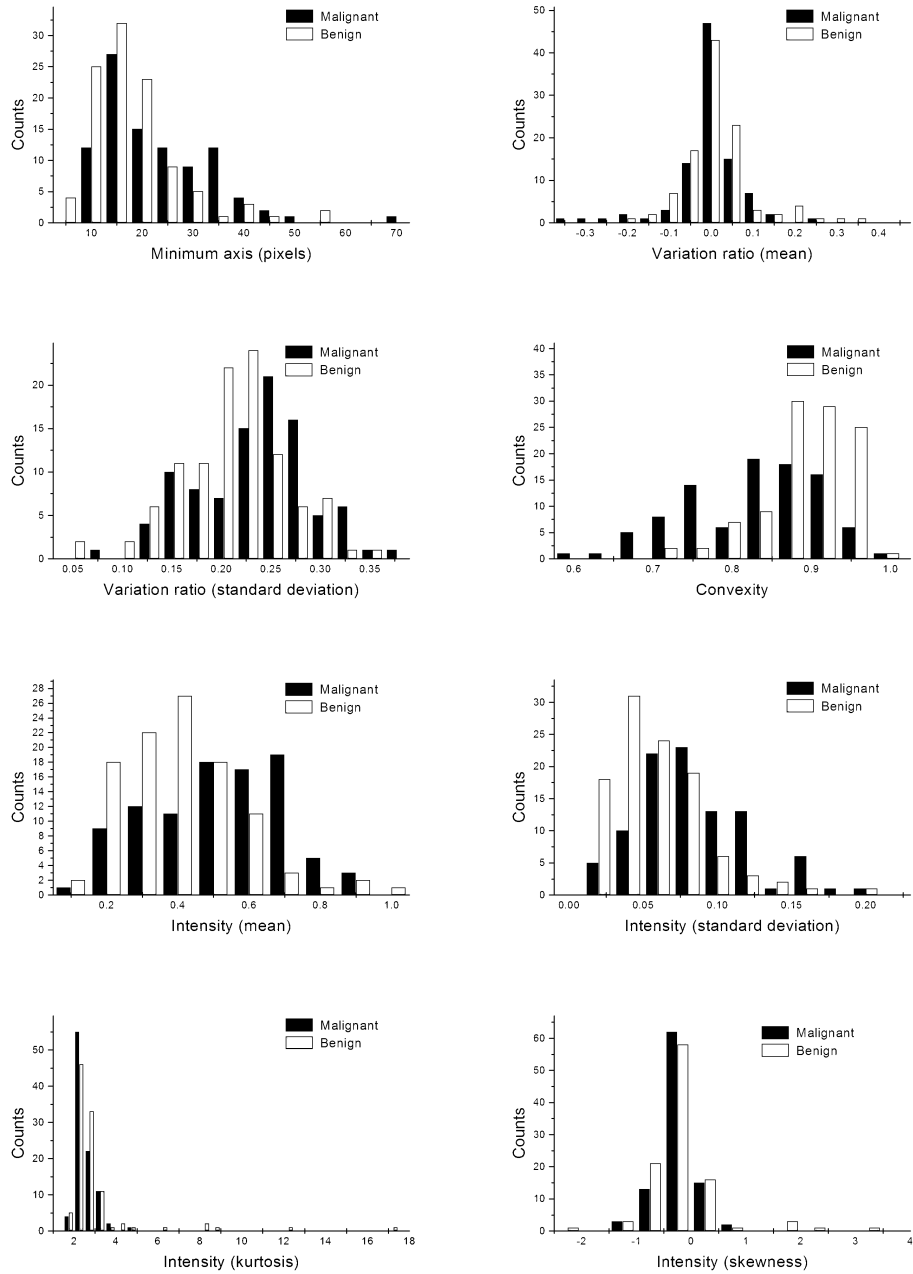


Figure 6: Distributions of the following features computed for malignant and benign masses: *minimum axis; mean and standard deviation of variation ratio; convexity; mean, standard deviation, kurtosis and skewness of the mass intensity.*

	1	2	3	4	5	6	7	8	9	10	11	12	13	14	15	16
1	100	91	-45	4	-12	-6	88	91	92	0	-8	-19	48	64	4	-25
2	91	100	-71	-14	0	11	98	96	93	0	7	-46	47	63	3	-19
3	-45	-71	100	58	-38	-54	-69	-65	-53	-7	-47	87	-22	-37	-4	-8
4	4	-14	58	100	-68	-84	-8	-16	11	-40	-65	64	10	1	0	-15
5	-12	0	-38	-68	100	91	1	6	-28	-15	78	-50	-17	-11	-5	18
6	-6	11	-54	-84	91	100	10	14	-18	0	82	-62	-13	-7	-2	19
7	88	98	-69	-8	1	10	100	94	92	-10	9	-46	45	61	1	-18
8	91	96	-65	-16	6	14	94	100	89	2	9	-40	49	66	4	-22
9	92	93	-53	11	-28	-18	92	89	100	-1	-16	-25	50	66	4	-24
10	0	0	-7	-40	-15	0	-10	2	-1	100	-20	-1	6	6	7	-6
11	-8	7	-47	-65	78	82	9	9	-16	-20	100	-59	-13	-8	-5	25
12	-19	-46	87	64	-50	-62	-46	-40	-25	-1	-59	100	-10	-26	2	-20
13	48	47	-22	10	-17	-13	45	49	50	6	-13	-10	100	74	-3	-35
14	64	63	-37	1	-11	-7	61	66	66	6	-8	-26	74	100	5	-10
15	4	3	-4	0	-5	-2	1	4	4	7	-5	2	-3	5	100	48
16	-25	-19	-8	-15	18	19	-18	-22	-24	-6	25	-20	-35	-10	48	100

Table 1: Matrix of the linear correlation coefficients $\rho(i, j)$ (expressed as percentages) among the 16 features. The features are numbered with $i = 1, \dots, 16$ according to the descriptions given in sec. 1.2.

The architecture of the three-layer feed-forward neural network we used consists in n input, 3 hidden and 2 output neurons, n depending on the choice of the number of features to be classified. We experimentally observed that the network performances for all choices of datasets are optimized with 3 neurons in the hidden layer.

Since the classifier performances and the comparison among different classifiers are conveniently evaluated in terms of the area A_z under the ROC curve, we reported in tab. 2 the estimated areas under the ROC curves obtained in each trial. The average A_z obtained on each test set and the standard deviation referred to the 10 different trials for each set of features are reported. As can be noticed, the performances the neural classifiers achieve are robust, i.e. almost independent of the partitioning of the available data into the train and test sets. The mean A_z value obtained in classifying 16, 15 and 12 features, i.e. in the *a*), *b*) and *d*) cases, are indeed very similar (p-values>0.05). Even in the *c*) case, where the less discriminating features are excluded from the set of features, the mean A_z value is not significantly different from those obtained with different choices of the features to be taken into account (p-values>0.05).

We can conclude that, being smaller but as predictive as the other sets of features, the *d*) set constituted by the 12 less correlated features will be considered as the optimal set of features to be extracted from segmented masses to determine their likelihood of malignancy.

The mean A_z value obtained with this system configuration on the sets of *correctly-segmented* masses is $A_z = 0.805 \pm 0.030$. The ROC curves realizing the minimum and maximum A_z values (0.756 and 0.849 respectively) are reported in fig. 7, where they are compared to the corresponding ROC curves achievable by running the CAD on the dataset of the *correctly-segmented* masses added by the 21 *acceptably-segmented* ones (column *e*) in tab. 2) and finally including also the 5 *non-acceptably-segmented* cases (column *f*) in tab. 2).

As shown in fig. 7, in the *d*) case high values as 80–85% of sensitivity to malignant masses correspond to specificity values in the 70–80% range.

Train set	Test set	a)	b)	c)	d)	e)	f)
		16 features 200 masses A_z	15 features 200 masses A_z	14 features 200 masses A_z	12 features 200 masses A_z	12 features 221 masses A_z	12 features 226 masses A_z
A_1	B_1	0.839	0.845	0.801	0.849	0.827	0.809
B_1	A_1	0.815	0.789	0.794	0.829	0.810	0.804
A_2	B_2	0.807	0.805	0.796	0.803	0.788	0.777
B_2	A_2	0.811	0.789	0.796	0.802	0.786	0.779
A_3	B_3	0.799	0.831	0.776	0.830	0.795	0.790
B_3	A_3	0.769	0.770	0.756	0.760	0.745	0.737
A_4	B_4	0.791	0.828	0.788	0.810	0.797	0.792
B_4	A_4	0.831	0.804	0.810	0.795	0.785	0.780
A_5	B_5	0.806	0.819	0.786	0.816	0.786	0.782
B_5	A_5	0.765	0.765	0.766	0.756	0.753	0.748
A_z mean		0.803	0.805	0.787	0.805	0.787	0.780
σ_{A_z}		0.024	0.026	0.017	0.030	0.024	0.023
A_z min		0.765	0.765	0.756	0.756	0.745	0.737
A_z max		0.839	0.845	0.810	0.849	0.827	0.809

Table 2: Evaluation of the performances of the neural classifiers trained on feature sets with different cardinalities: the A_z values obtained on the test sets according to the 5×2 cross validation method are reported.

3.4 The reject option

As the segmentation algorithm leads to three classes of segmented masses according to the radiologist’s evaluation, we considered the opportunity of exploiting this quality control performed on the segmentation step of the analysis to minimize the amount of cases misclassified by the neural decision-making system. We adopted the *reject option* [41, 42], i.e. we evaluated the convenience of not assigning a class to the input sample (rejection of the sample), rather than risking a wrong classification. A suitable criterion for rejection has to reject the highest possible percentage of samples which would be otherwise misclassified. The *reject option* is based on an estimate of the classification reliability, measured by a *reliability evaluator* Ψ . Once a *reject threshold* σ has been fixed, a sample is rejected if the corresponding value of Ψ is below σ . We set a trivial correspondence between the values assumed by the Ψ function and the radiologist’s opinion about the quality of mass segmentation: $\Psi = 1$ for *correctly-segmented* masses, $\Psi = 0.5$ for *acceptably-segmented* masses and $\Psi = 0$ for *non-correctly-segmented* masses. In other words, the Ψ function is directly determined by the radiologist, rather than being implemented as a function to be automatically derived from data. Only two possible classes of values for the threshold σ make sense in this case: $0 < \sigma_a < 0.5$ and $0.5 < \sigma_b < 1$. If σ_a is set as *reject threshold*, the *correctly-segmented* masses and the *acceptably-segmented* ones (corresponding to the ϵ_{CS+AS} fraction of the dataset) will be classified by the system; otherwise, if σ_b is chosen, only the *correctly-segmented* masses (the ϵ_{CS} fraction of the cases) will be classified, whereas the remaining cases will be rejected.

As reported in columns *d)* and *e)* of tab. 2, the mean A_z value obtained in case the ϵ_{CS+AS} fraction of cases is classified does not significantly differ from the mean A_z computed on the ϵ_{CS} fraction of cases ($p=0.16$). It means that it is not worth setting a *reject threshold* as severe as σ_b , since it will only lead to a reduction of the rate of reliably classified cases, without improving the classification reliability. By contrast, the comparison between the mean A_z value obtained on the sets including the *non-correctly-segmented* masses reported in column *f)* and the mean A_z of column *d)* shows a statistically significant difference ($p=0.048$). Despite this conclusion is achieved on

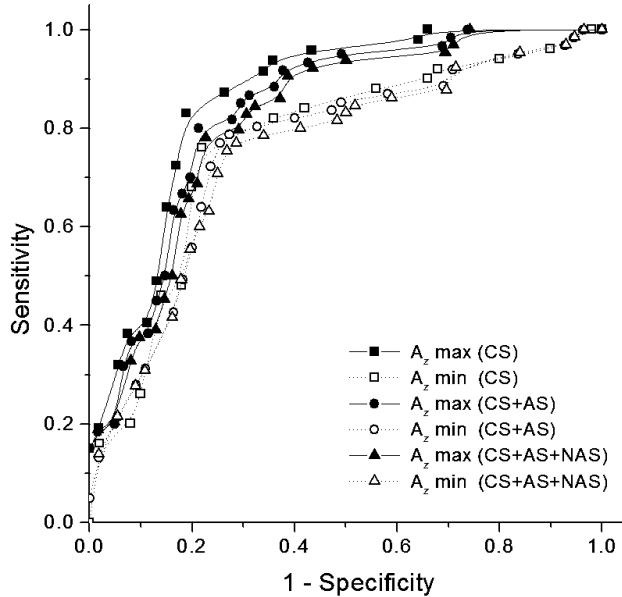


Figure 7: ROC curves obtained in the classification of 12 features (see tab. 2) extracted from the datasets of: *correctly-segmented* masses (CS); *correctly-segmented* and *acceptably-segmented* masses (CS+AS); *correctly-segmented*, *acceptably-segmented* and *non-acceptably-segmented* masses (CS+AS+NAS).

the basis of a borderline p value, the choice of σ_a as *reject threshold* will preserve the system performances from a slight decrease due to the possible failure of the mass segmentation step. Once the *reject threshold* σ_a is applied to the system, a small subset of masses will be initially rejected as the segmentation algorithm did not lead to an acceptable result; however, the radiologist in this case has the advantage that he can more safely trust the stability and reliability of the CAD performances on the remaining ϵ_{CS+AS} fraction of the cases.

4 Conclusions and discussion

We developed a CAD system for the classification of mammographic masses into malignant and benign with the aim of supporting radiologists in the visual diagnosis of the degree of mass malignancy. Several expert systems with a similar purpose have been recently discussed in the literature. In the paper by Timp and Karssemeijer [15] the influence of the segmentation method on the performance of a CAD system was investigated, obtaining $A_z = 0.74, 0.72$ and 0.67 for segmentation based on dynamic programming, on the discrete contour model and on region growing, respectively. Kinnard *et al.* [17] studied the efficacy of image features versus likelihood features of tumor boundaries for differentiating benign and malignant tumors; a region growing technique was implemented in the mass segmentation and two different neural networks were adopted in the classification. Different combinations of these components led to $A_z = 0.66, 0.71$ and 0.84 , respectively. Mudigonda *et al.* [23] compared the discriminating capabilities of gradient-based and texture-based features. Different classification approaches on different sets of mammograms led to $A_z = 0.85, 0.67, 0.6, 0.76, 0.52$ and 0.73 . Hadjiski *et al.* [33] developed a hybrid classifier by combining an unsupervised model based on an adaptive resonance theory network and a supervised linear discriminant classifier. They reached the value $A_z = 0.81$ for the hybrid classifier to be compared to $A_z = 0.78$ and 0.80 obtained by means of the linear discriminant classifier alone and

a back-propagation neural network respectively. Huo *et al.* [24] implemented a region growing technique to segment masses and extracted radial edge-gradient information to gather the mass malignancy, obtaining $A_z = 0.85$. Sahiner *et al.* [22] developed a three-stage segmentation method based on clustering, active contour and spiculation detection. They evaluated the improvement the extraction of morphological features can lead to a mass classification based on texture features extracted from a band of pixels surrounding the mass. They obtained $A_z = 0.83 \pm 0.02$, 0.84 ± 0.02 and 0.87 ± 0.02 on morphological, texture and combined features, respectively. They also combined the analysis of different views of a mass, obtaining $A_z = 0.91 \pm 0.02$. The issue of improving the classification performances in the mass diagnosis is discussed in the paper by Lim and Er [34], where generalized dynamic fuzzy neural networks are introduced. In this case, the most appropriate structure for the classifier is automatically obtained by means of a self-adapting of the network structure during the learning process. In classifying mammographic masses they obtain $A_z = 0.868 \pm 0.020$. Hadjiiski *et al.* [21] exploited the interval change information to evaluate the mass malignancy. The information on the prior image significantly improved the accuracy of mass classification from $A_z = 0.82$ to $A_z = 0.88$. Another paper by Sahiner *et al.* [13] discussed the effect of mass segmentation on characterization: texture, morphological and spiculation features were extracted from masses segmented by a computerized technique and by the radiologist, obtaining $A_z = 0.89$ and 0.88 , respectively. Sahiner *et al.* in a different work [10] transformed a band of pixels surrounding a segmented mass into the Cartesian plane. They computed and classified texture features of the transformed images, ending up with $A_z = 0.94$. In another study by Huo *et al.* [8], three different automated classifiers were used to merge various features related to the margin and density of the masses into a likelihood of malignancy, obtaining $A_z = 0.94$.

Despite the area A_z under the ROC curve provides a good measuring instrument to make a comparison among the performances of different CAD systems, the reliability of this measurement depends also on the dataset used to train and test the CAD. It is very difficult in most cases to evaluate how a particular database is well populated, i.e. whether it is sufficiently representative of each possible appearance of the pathology one aims to detect. Even the partitioning of the database into train and test sets is not a trivial task: one should at least *a posteriori* verify the robustness of the results achieved with respect to different data partitioning.

The CAD system we present in this paper has been developed according to all these considerations. The performances it reaches are in the same range of most of the previously reported results. We devoted the main efforts to the development of the mass segmentation step. We significantly improved the procedure proposed by Chen *et al.* [16] for the analysis of sonograms, by making the algorithm iterative. In particular, as mammographic images show a better resolution with respect to sonograms, an appropriate segmentation procedure needs to be particularly sensitive even to subtle variations occurring in the mass margins. The iterative procedure we propose is able to identify even very small arms and branches possibly occurring especially in malignant masses. Furthermore, it has the ability of handling masses with various sizes: there is no size limit even up to few pixels. The algorithm execution is not computationally expensive; computation time has linear relation with the size of the mass. In contrast with the analysis by Chen *et al.* [16] we could not find any improvement in the mass margin definition and consequently in the final CAD results by introducing the wavelet transforms in the identification of the critical points defining the mass margin.

Despite the accuracy of segmentation algorithms is usually evaluated in terms of the overlap between the area segmented by the CAD and the manual segmentation of the mass provided by an experienced radiologist, we have not had the possibility to carry out such a study. To test the reliability of our segmentation procedure we adopted the following criterion: the radiologist partitioned the segmented masses in three classes, according to a decreasing rate of reliability of the segmentation result; the CAD performances were evaluated first on the dataset of *correctly-segmented* masses, obtaining $A_z = 0.805 \pm 0.030$; then, also *acceptably-segmented* and *non-correctly-segmented* masses (which represent however small fractions of the dataset) were added in two steps to the test sets, obtaining $A_z = 0.787 \pm 0.024$ and 0.780 ± 0.023 , respectively. As the differ-

ence among the A_z values obtained on the fraction $\epsilon_{CS} = 88.5\%$ of *correctly-segmented* masses and the fraction $\epsilon_{CS+AS} = 97.8\%$ of *correctly-* and *acceptably-segmented* cases is not statistically significant, we can conclude that even in case the segmentation does not provide an extremely refined identification of the mass margin, the interplay between the morphological and textural features extracted from the segmented area still leads to a reliable classification result on the 97.8% of the database.

Acknowledgments

We would like to thank the professors, the radiologists and the employees of the Radiological Departments who contributed to the acquisition of the mammographic database in the framework of the INFN-founded CALMA Project. We are grateful to Dr S. Franz from ICTP (Trieste, Italy) for useful suggestions and discussions. Special thanks to Dr M. Tonutti from Cattinara Hospital (Trieste, Italy) for her essential contribution in the evaluation of the efficiency of the segmentation algorithm.

References

- [1] R.T. Greenlee, M.B. Hill-Harmon, T. Murray and M. Thun, Cancer statistics, *Ca-Cancer J Clin* **51**(1) 15–36 (2001). Erratum in: *Ca-Cancer J Clin* **51**(2) 144 (2001).
- [2] F. Levi, F. Lucchini, E. Negri, W. Zatonski, P. Boyle and C. La Vecchia, Trends in cancer mortality in the European Union and accession countries, 1980-2000, *Ann. Onc.* **15**(9) 1425–1431 (2004).
- [3] R.A. Smith, The epidemiology of breast cancer, *Syllabus: A Categorical Course in Breast Imaging*, Radiological Society of North America, pp. 7–20. D.B. Kopans and E.B. Mendelson eds (1995).
- [4] S.H. Landis, T. Murray, S. Bolden and P.A. Wingo, Cancer statistics, 1999. *Ca-Cancer J Clin* **49**(1) 8–31 (1999).
- [5] H.C. Zuckerman, The role of mammography in the diagnosis of breast cancer, *Breast cancer: diagnosis and treatment*, pp. 152–72. I.M. Ariel and J.B. Cleary eds, New York: McGraw-Hill (1987).
- [6] A.G. Haus and M.J. Yaffe eds, *Syllabus: A Categorical Course in Physics - Technical Aspects in Breast Imaging*, Radiological Society of North America, Presented at the 79th Scientific Assembly and Annual Meeting of RSNA (1993).
- [7] D.D. Adler and M.A. Helvie, Mammographic biopsy recommendations, *Curr Opin Radiol* **4**(5) 123–9 (1992).
- [8] Z. Huo, M.L. Giger, C.J. Vyborny, D.E. Wolverton, R.A. Schmidt and K. Doi, Automated computerized classification of malignant and benign masses on digitized mammograms, *Acad Radiol* **5**(3) 155–68 (1998).
- [9] Z. Huo, M.L. Giger, C.J. Vyborny, D.E. Wolverton and C.E. Metz, Computerized classification of benign and malignant masses on digitized mammograms: a study of robustness, *Acad Radiol* **7**(12) 1077–84 (2000).
- [10] B. Sahiner, H.P. Chan, N. Petrick, M.A. Helvie and M.M. Goodsitt, Computerized characterization of masses on mammograms: the rubber band straightening transform and texture analysis, *Med Phys* **25**(4) 516–26 (1998).
- [11] M.A. Wirth and A. Stapinski, Segmentation of the Breast Region in Mammograms Using Active Contours, *Visual Communications and Image Processing* **5150**, pp. 1995–2006. T. Ebrahimi and T. Sikora eds, Lugano, Switzerland (2003).
- [12] A. Amini, S. Tehrani and T. Weymouth, Using Dynamic programming for Minimizing the Energy of Active Contours in the Presence of Hard Constraints, *Proc Second Int Conf Computer Vision*, pp. 95–99. Tarpon Springs, FL (1988).

- [13] B. Sahiner, N. Petrick, H.P. Chan, L.M. Hadjiiski, C. Paramagul, M.A. Helvie and M.N. Gurcan, Computer-Aided Characterization of Mammographic Masses: Accuracy of Mass Segmentation and Its Effects on Characterization, *IEEE Trans Med Imaging* **20**(12) 1275–84 (2001).
- [14] M.A. Kupinski and M.L. Giger, Automated Seeded Lesion Segmentation on Digital Mammograms, *IEEE Trans Med Imaging* **17**(4) 510–17 (1998).
- [15] S. Timp and N. Karssemeijer, A new 2D segmentation method based on dynamic programming applied to computer aided detection in mammography, *Med Phys* **31**(5) 958–71 (2004).
- [16] D.R. Chen, R.F. Chang, W.J. Kuo, M.C. Chen and Y.L. Huang, Diagnosis of Breast Tumors with Sonographic Texture Analysis using Wavelet Transform and Neural Networks, *Ultrasound Med Biol* **28**(10) 1301–10 (2002).
- [17] L. Kinnard, S.B. Lo, P. Wang, M.T. Freedman, M. Chouikha, Separation of Malignant and Benign Masses Using Image and Segmentation Features, *Medical Imaging 2003: Image Processing* **5032** 835–842 (2003).
- [18] L.M. Kinnard, S.C.B. Lo, P.C. Wang, M.T. Freedman and M.F. Chouikha, Separation of malignant and benign masses using maximum-likelihood modeling and neural networks, *Proc. SPIE* **4684** pp. 733–741. *Medical Imaging 2002: Image Processing*, M. Sonka and J.M. Fitzpatrick eds (2002).
- [19] I. Christoyianni, E. Dermatas and G. Kokkinakis, Neural Classification of Abnormal Tissue in Digital Mammography using Statistical Features of the Texture, *IEEE, ICECS'99* **1** 117–120 (1999).
- [20] W. Qian, L. Li and L.P. Clarke, Image Feature Extraction for Mass Detection in Digital Mammography: Influence of Wavelet Analysis, *Med Phys* **26** 402–408 (1999).
- [21] L. Hadjiiski, B. Sahiner, H.P. Chan, N. Petrick, M.A. Helvie and M. Gurcan, Analysis of temporal changes of mammographic features: computer-aided classification of malignant and benign breast masses, *Med Phys* **28**(11) 2309–17 (2001).
- [22] B. Sahiner, H.P. Chan, N. Petrick, M.A. Helvie and L.M. Hadjiiski, Improvement of mammographic mass characterization using spiculation measures and morphological features, *Med Phys* **28**(7) 1455–65 (2001).
- [23] N.R. Mudigonda, R.M. Rangayyan and J.E. Desautels, Gradient and texture analysis for the classification of mammographic masses, *IEEE Trans Med Imaging* **19**(10) 1032–43 (2000).
- [24] Z. Huo, M.L. Giger, C.J. Vyborny, U. Bick, P. Lu, D.E. Wolverton and R.A. Schmidt, Analysis of spiculation in the computerised classification of mammographic masses, *Med Phys* **22**(10) 1569–1579 (1995).
- [25] American College of Radiology. Breast Imaging - Reporting and Data System (BI-RADS®), 3rd ed. Reston, VA: American College of Radiology (1998), <http://www.birads.at/>
- [26] T. Lambrou, A.D. Linney, R.D. Speller, A. Todd-Pokropek, Statistical Classification of Digital Mammograms Using Features from the Spatial and Wavelet Domains, 2nd *European Medical and Biological Engineering Conference (EMBECE)*, Vienna, Austria (2002).
- [27] L.M. Bruce and R.R. Adhami, Classifying Mammographic Mass Shapes Using the Wavelet Transform Modulus-Maxima Method, *IEEE Trans Med Imaging*, **18**(12) 1170–77 (1999).
- [28] D. Wei, H. Chan, M.A. Helvie, B. Shiner, N. Petrick, D.D. Adler and M.M. Goodstitt, Classification of Mass and Normal Breast Tissue on Digital Mammograms: Multiresolution Texture analysis, *Med Phys* **22**(9) 1501–13 (1995).
- [29] S. Liu, C.F. Babbs and E.J. Delp, Multiresolution Detection of Spiculated Lesions in Digital Mammograms, *IEEE Trans Image Processing* **10**(6) 874–884 (2001).

- [30] L. Arbach, D.L. Bennett, J.M. Reinhardt and G. Fallouhc , Classification of Mammographic Masses: Comparison between Backpropagation Neural Network (BNN) and Human Readers, *Medical Imaging* **5032** 810–818 (2003).
- [31] A. Lauria, R. Palmiero, P. Cerello, B. Golosio, F. Fauci, R. Magro, G. Raso, S. Tangaro, P.L. Indovina, The CALMA system: an Artificial Neural Network Method for Detecting Masses and Microcalcifications in Digitized Mammograms, *Nucl Instr Meth A* **518** 391–393 (2004).
- [32] K. Bovis and S. Singh, Classification of Mammographic Breast Density Using a Combined Classifier Paradigm, *Medical Image Understanding and Analysis (MIUA) Conference*, Portsmouth (2002).
- [33] L. Hadjiski, B. Sahiner, H.P. Chan, N. Petrik and M. Helvie, Classification of Malignant and Benign Masses Based on Hybrid ART2LDA Approach, *IEEE Trans Med Imaging* **18**(12) 1178–87 (1999).
- [34] W.K. Lim and M.J. Er, Classification of mammographic masses using generalized dynamic fuzzy neural networks, *Med Phys* **31**(5) 1288–95 (2004).
- [35] S. Haykin, *Neural Networks: a Comprehensive Foundation*, Macmillan College Publishing Company, New York, 1994.
- [36] T.G. Dietterich, Approximate Statistical Test For Comparing Supervised Classification Learning Algorithms, *Neural Computation* **10**(7) 1895–923 (1998).
- [37] M. Stone, Cross-validatory choice and assessment of statistical predictions, *Journal of Royal Statistical Society B* **36** 111–147 (1974).
- [38] C.E. Metz, ROC methodology in radiologic imaging, *Invest Radiol* **21**(9) 720–33 (1986).
- [39] U. Bottigli, P. Delogu, M.E. Fantacci, F. Fauci, B. Golosio, A. Lauria, R. Palmiero, G. Raso, S. Stumbo and S. Tangaro, Search of microcalcification clusters with the CALMA CAD station, *The International Society for Optical Engineering (SPIE)* **4684** 1301–10 (2002).
- [40] R. Bellotti, S. Bagnasco, U. Bottigli, M. Castellano, R. Cataldo, E. Catanzariti, P. Cerello, S.C. Cheran, F. De Carlo, P. Delogu, I. De Mitri, G. De Nunzio, M.E. Fantacci, F. Fauci, G. Forni, G. Gargano, B. Golosio, P.L. Indovina, A. Lauria, E. Lopez Torres, R. Magro, D. Martello, G.L. Masala, R. Massafra, P. Oliva, R. Palmiero, A. Preite Martinez, R. Prevete, M. Quarta, L. Ramello, G. Raso, A. Retico, M. Santoro, M. Sitta, S. Stumbo, S. Tangaro, A. Tata and E. Zanon, The MAGIC-5 Project: Medical Applications on a Grid Infrastructure Connection, *IEEE Nuclear Science Symposium Conference Record* Vol. **3** 1902–1906 (2004).
- [41] C. De Stefano, C. Sansone and M. Vento, To reject or not to reject: that is the question-an answer in case of neural classifiers, *IEEE Transactions on Systems, Man and Cybernetics, Part C* **30**(1) 84–94 (2000).
- [42] G.C. Vasconcelos, M.C. Fairhurst and D.L. Bisset, Investigating feedforward neural networks with respect to the rejection of spurious patterns, *Pattern Recognit Lett* **16**(2) 207–212 (1995).